Cite as: H. Yang *et al.*, *Science*
10.1126/science.aed5665 (2026).

Cyclic sealing and drainage on an oceanic transform fault

Hao Yang[1], Lingling Ye[2], Haijiang Zhang[1,3]*

[1]Key Laboratory of Precision Geodesy, School of Earth and Space Sciences, University of Science and Technology of China, Hefei, China. [2]Department of Earth and Space Sciences, Southern University of Science and Technology, Shenzhen, China. [3]Mengcheng National Geophysical Observatory, University of Science and Technology of China, Mengcheng, China.

*Corresponding author. E-mail: zhang11@ustc.edu.cn (H.Z.)

Oceanic transform faults have been considered conservative, shear-dominated boundaries, yet their proximity to magmatic systems implies fluid involvement. Here, we discovered tidally modulated tremor at the Gofar transform fault along the East Pacific Rise. Tremor amplitude correlates with semidiurnal tides during periods of sparse seismicity and low in-situ compressional to shear wave velocity ratio (Vp/Vs), but this correlation weakens following earthquake swarms accompanied by high Vp/Vs. We propose a valve-like sealing–drainage dynamic process where sealing traps volatiles and boosts tidal sensitivity, sustaining tremor activity until rupture opens high porosity and permeability pathways, which silences tremors, triggers microseismicity, and resets the system via hydrothermal resealing. Thus, transform faults are likely permeable and tide-critical, with energy release oscillating between tremors and rupture, paced by magmatic volatile supply and healing.

Oceanic transform faults, which accommodate strike-slip motion between offset mid-ocean ridge segments, have long been viewed as conservative plate boundaries dominated by simple shear and largely devoid of magmatic input. This two-dimensional (2D) paradigm, established since the advent of plate tectonic theory (*1*), has been increasingly challenged by observations of pronounced structural heterogeneity, magmatic intrusions, and active hydrothermal circulation at ridge-transform intersections (*2*–*4*). High-resolution geophysical images reveal that these faults are not simple planes but complex 3D damage zones, with fault architecture and material properties varying strongly along strike (*5*, *6*). This structural complexity, particularly in the shallow crust, provides a hydrothermal plumbing system that links deep magmatic volatiles to the seafloor, suggesting a dynamic fault zone where fluids play a critical role in the seismic cycle (*7*, *8*).

A key to understanding these fluid–rock interactions is tremor—a sustained, non-impulsive seismic signal characterized by narrow-band and often harmonic spectra that lasts from minutes to days (*8*–*11*). In subduction zones and volcanic systems, tremor is highly sensitive to kilopascal-level stress perturbations, such as those from tides, and is commonly linked to pressurization and fluid flow within critically stressed fractures (*8*–*11*). The presence of tremor on mid-ocean ridges and submarine volcanoes, as well as its synchronization with tidal cycles, indicate that shallow fracture networks can amplify weak periodic stresses into observable tremor responses (*12*–*15*). However, it remains unclear whether comparable tidally modulated tremor occurs within oceanic transform faults, and how any such tremor relates to fault-zone properties and microseismicity.

The Gofar transform fault on the East Pacific Rise (EPR) slips at ~14 cm yr^{-1}. At its western G3 segment, M6 ruptures recur quasi-periodically every 5–6 years on two ~15-km-long rupture patches separated along strike by a ~10-km-long seismic barrier that has prevented rupture propagation from M6 earthquakes on both sides but hosts abundant microseismicity extending to the uppermost mantle (*16*) (Fig. 1). Various evidence from wide-angle seismic refraction imaging (*17*, *18*), seismicity analysis using local dense arrays (*19*–*23*), controlled-source electromagnetic inversion (*24*), and dynamic source modeling (*21*) indicate that elevated deep fluids and/or intensified fault damage most likely generate and sustain this seismic barrier zone.

Here, we report the discovery of tidally modulated harmonic tremor in the seismic barrier zone of the Gofar transform fault, using data from a dense array of ocean-bottom seismometers (OBS). We show that the tremor amplitude closely tracks semidiurnal tides, although this coupling abruptly breaks down following moderate M4 earthquake ruptures. The period of strong tremor–tide correlation coincides with lower seismicity rate and a gradual drop in Vp/Vs. In contrast, when the correlation breaks down, we observed an increase in microseismicity and a rapid rebound in Vp/Vs. We interpret these observations as evidence for cyclic sealing and drainage processes occurring within the oceanic transform fault, governed by the coevolution of fault-zone permeability and pore pressure: progressive hydrothermal sealing traps volatiles, amplifying tidal stresses and sustaining tremors until earthquake rupture reconnects fluid pathways, drains fluids, and resets the system. This valve-like mechanism recasts transform faults from passive shear boundaries into active, fluid-controlled 3D systems where energy release is paced by the interplay of tidal loading, fluid migration, and variations in fault-zone permeability.

Tidal modulation of harmonic tremor

We identified persistent, harmonic tremor signals characterized by emergent onsets (signals begin gradually and increase in amplitude slowly) and durations from tens of minutes to hours (Fig.

2, A and B) from continuous waveforms of a dense OBS array deployed at the G3 segment of the Gofar transform fault (*25*). The tremor exhibited a stable spectral structure with a fundamental frequency range of ~2–8 Hz (Fig. 2, B, D, and E), consistent with the narrowband signature typical of fluid-induced resonance (*9*, *12*). The tremor signal weakened markedly following an M4.0 earthquake on 8 September 2020 (marked as event E2 in Fig. 1; Fig. 2, A to C), indicating a natural subsurface origin rather than ship or oceanic noise. The OBS array indicates a mixed tremor origin produced by the superposition of shallow, complex, small-amplitude sources (fig. S1). Its narrowband, intermittent energy release and variations among stations reflect localized sources related to oscillations of fluid-filled cracks or boiling-induced cavities, with multiple weak radiators superposed in the near field rather than a single compact source. Resonance of these radiators can be sensitively modulated by small external stress perturbations by opening/closing cracks and altering fluid pathways (*9*, *26*), consistent with observations at the 9°50′N EPR and Brothers volcanic hydrothermal systems (*12*, *14*).

We located tremor sources using a waveform-migration method with a semblance-based imaging condition, well suited for detecting and locating continuous narrowband tremor signals (*27*, *28*). The inferred sources lie within ~4.5 km below the seafloor and nearly coincide with the previously inferred barrier region along the G3 segment of the Gofar transform fault (Figs. 1B, S2-S5; see Methods).

The root-mean-square (RMS) amplitude of tremor in the 2–8 Hz band varies systematically with the calculated total tidal volume strain including contributions from solid Earth tide (or body tide referred to in ref. *29*), regional ocean-mass loading, and direct water-column loading (fig. S6; see methods). The M2 tidal constituent (~12.4 hours) is the dominant contributor to the total tidal volume strain in the study area, and the two are almost coincident except for some slight differences in amplitude (fig. S7). Thus, we used the M2 tidal constituent to analyze the correlation between tidal and RMS time series. Before the E2 rupture, the RMS amplitude exhibited an evident semidiurnal modulation with a slight but resolvable phase lag (Fig. 2C). In contrast, after the M4.0 E2 earthquake this modulation broke down, and the RMS amplitude was dominated by short-lived, high-amplitude spikes related to local microearthquakes (Fig. 2C). Amplitude spectral densities (after excluding detected earthquake signals) show elevated 2–8 Hz energy during the tremor-tide correlation interval but strongly reduced 2–8 Hz power during the decorrelation interval (Fig. 2D). The 2-hour time series before the M4 earthquake further reveals more sustained narrowband, harmonic energy versus weaker, intermittent tremor-band energy afterward (Fig. 2E). This tremor-tide correlation is observed across the array, and is generally stronger in station clusters A1 and A2 than in A3 (fig. S8), indicating lateral heterogeneity in tremor source strength.

Semidiurnal periodicity is clearly expressed in both the frequency and phase domains (Fig. 3; see methods). After removing time windows containing detected earthquakes, periodogram of the tremor RMS time series during the tremor–tide correlation interval displays a dominant spectral peak precisely at the M2 period in the station-averaged spectrum (Fig. 3A and fig. S8A). Weaker but distinct diurnal peaks at K1 and O1 are also present. During the correlation interval, pairwise correlations of RMS time series are high (fig. S9A). In the decorrelation interval, these tidal peaks are strongly reduced (Fig. 3A and fig. S8B), and pairwise station correlations drop markedly (fig. S9B). During the correlation interval, the tremor RMS series traces a harmonic curve fitting the M2 tidal signals, with a high cross-correlation coefficient of 0.92 and a phase lag of -21.0°, whereas the decorrelation interval is nearly flat with low similarity to the tidal curve (Fig. 3B). Similar disruption-and-recovery cycles occurred during three additional intervals associated with M~4 earthquakes in 2020, and the inferred phase lags vary among episodes (figs. S10 and S11).

Breakdown and recovery of tremor-tide correlation after rupture

The tremor–tide correlation breaks down after the M4 earthquake rupture, revealing a dynamic valve-like mechanism. The system's response to the M4.0 earthquake rupture on 8 September 2020 (E2) provides a sensitive test of the tidal coupling framework. Across the array, tremor–tide correlation collapses (Fig. 3 and fig. S8B). Concurrently, the inter-station correlation across the array breaks down (fig. S9B), indicating a fundamental change in tremor-generating processes.

We detected and relocated the events during the observation period (fig. S12; see methods). Before event E2, seismicity rate dropped together with b-values and in-situ Vp/Vs ratios (Fig. 4; see methods). The decrease of Vp/Vs can be interpreted as a transition toward a more gas-rich pore system. Gas is highly compressible, so it lowers the effective fluid bulk modulus and preferentially reduces P-wave speed, thus lowering Vp/Vs, whereas liquid-dominated cracks yield higher Vp/Vs (*30*, *31*). This interpretation is consistent with sustained, deep-magma degassing feeding the shallow hydrothermal network, and similar gas-liquid control on Vp/Vs has been reported in volcanic-hydrothermal settings (*32*). The gas-rich state of the fracture network suggests that the system is in a sealing stage. The decreasing trend in b-value, along with lower seismicity rate, also indicates a progressive buildup of shear stress as the shallow fracture network tightens and sealing advances. After the E2 rupture, this pattern reversed abruptly: seismicity intensified, b-value rebounded, and Vp/Vs rose transiently (Fig. 4), marking rupture-driven opening of the sealed system. The increase in b-value suggests more distributed cracking, whereas the Vp/Vs jump indicates rapid hydraulic reconnection and fluid recharge, with gases escaping in newly opened fractures. Together, these features indicate a transient, stress-driven increase in permeability that disrupted the tidal coupling at the tremor sources. Alternative explanations for elevated Vp/Vs, such as crack closure, pore collapse, or thermal transients, are unlikely because they cannot simultaneously account for the contemporaneous rise in both b-value and seismicity on this timescale.

This breakdown of the tremor-tide correlation after the E2 rupture is a direct manifestation of the anticipated "valve-opening" event. The coseismic rupture and subsequent fracturing from aftershocks transiently increased fault-zone porosity and permeability, enhancing hydraulic connectivity and accelerating pore-pressure equilibration, thereby reducing pore-pressure retention and weakening the transmission of tidal loading to the crack system. Consequently, the tremor, while sometimes present, lost its tidal correlation. In fact, the correlation of tremor RMS and tidal signals started to decrease about 3 days before the E2 mainshock (Fig. 2A), indicating the system may have already experienced some aseismic slip to facilitate the drainage of fluid and gases.

In the weeks following the E2 rupture, as aftershock activity decays, tidal modulation gradually re-emerges (fig. S15, A to E). This recovery occurred on a timescale controlled by chemical–mechanical sealing processes, such as pressure solution and mineral precipitation (e.g., silica, carbonates), which reduce permeability (*7*, *33*). As the system resealed, pore pressure rebuilt and the gas fraction increased, leading to a gradual reduction in Vp/Vs. Strengthening tremor–tide correlation thereby tracks the progressive reloading process. The fault zone returned to a near-critical state with near-lithostatic pore pressure, where the semidiurnal tide could again efficiently pump the tremor sources. Following a later M4.3 rupture on 27 November 2020 (E4), tremor–tide correlation again diminished, indicating a renewed permeability increase that weakened the tidal coupling (fig. S15F).

We further evaluated the behaviors of the system during other nearby M4 earthquakes within the observation period and found that the 11 August 2020 M4.1 earthquake (event E1) only caused a negligible effect on the tremor-tide coupling (Fig. 2 and fig. S16) compared to event E2. Seismic waveforms of both E1 and E2 (fig. S17) exhibit low-frequency or mixed-band characteristics, indicating fluid involvement and longer source durations (*34*). The key difference is that E2 occurred within the tremor source zone and ruptured the shallow damage zone (Fig. 1 and fig. S10), thereby producing much stronger disruption of tremor–tide correlation than E1. By contrast, E1 was located farther away from the tremor zone and may have primarily affected deeper magmatic depressurization and degassing, with little effect on the tremor zone. The other three earthquakes (D1, D2 and E4) occurring within the tremor zone also produced stronger disruption of the tremor–tide correlation (fig. S11) comparable to event E2.

This observed sequence—(i) sealed conditions with tremor-tide correlation, low seismicity and Vp/Vs; (ii) rupture-associated loss of tremor-tide correlation, a microseismicity surge, and increased Vp/Vs; and (iii) gradual resealing and recovery of tremor-tide correlation—captures a complete cycle of shallow transient permeability and pore pressure evolution in the barrier zone of the Gofar transform fault. It reveals that the oceanic transform fault zone dynamically toggles between two states: a sealed, pressurized, tremor-prone state and a ruptured, high-permeability, small earthquake-prone state.

Pore pressure response of the transform fault to tides

Within a poroelastic framework, tidal loading perturbs pore pressure through coupled skeletal volume change and pore-fluid compression/transport (*35*, *36*). Combining mass conservation with Darcy's law and linearizing for small perturbations yields a first-order evolution equation for the pore pressure response (see methods). We constructed a physically reasonable model in which the mainshock rupture briefly reconnects fractures or fluid pathways, represented as a step increase in permeability k (fig. S18A). Permeability then gradually recovers as chemical sealing, mineral precipitation, and particle re-bridging proceed, as observed and experimentally demonstrated (*37*, *38*). Using the tidal volume strain as input, we forward modeled the pore-pressure response and compared it with the observed M2 modulation (fig. S18, B and C).

The model reproduces two key observations. Before rupture, the fault is relatively sealed (low k), and pore pressure responds to the semidiurnal cycle in a regime dominated by local pore spaces with limited diffusion, producing strong modulation relative to the tidal volume strain with a cross-correlation coefficient of 0.97 and phase lag of -21.0°, consistent with the observed phase lag (Fig. 3B). The negative phase lag arises from the model's diffusive flow component: as the strain rate decreases, the response becomes more drainage-dominated, causing pore pressure to peak before the tidal volume strain and producing a phase lag of -90° to 0°, which is controlled by a characteristic diffusion timescale. After rupture, increased permeability allows pore-pressure perturbations to diffuse and equilibrate more readily within the connected fracture network, thereby reducing the amplitude of tidal modulation (fig. S18B). This change also alters the relative contribution of the instantaneous loading and time-dependent flow components of the pore-pressure response, yielding a more negative phase lag relative to the volume strain (fig. S18C).

We further connected the pore-pressure response to fluid-induced resonance of the tremor energy. As the fault approaches a near-critical state with fluid/gas enrichment, the progressive buildup of pore pressure reduces the effective normal stress, allowing semidiurnal tidal perturbations at about 10 kPa level to strongly modulate whether resonance is excited and how efficiently it radiates (*11*). Near this excitation threshold, kPa-level tidal stressing can slightly open or clamp fractures and change how easily fluid moves through them, so the crack or cavity oscillations can turn on and off and their amplitude can vary strongly, while the dominant frequency changes little because it is mainly set by fracture length and shape as well as fluid viscosity (*9*, *26*). This process explains the pronounced semidiurnal modulation in the pre-rupture tremor energy that we observed on the Gofar transform fault and is comparable to observations of tremor being highly sensitive to small tidal stresses on weak faults in subduction settings (*39*). After rupture, the near-critical state is disrupted. The increase in permeability allows pore-pressure perturbations to equilibrate more readily within the connected fracture network, thereby reducing the amplitude of tidal pore-pressure modulation and weakening tremor-tide correlation; as sealing progresses and stress accumulates, the system gradually returns toward a near-critical state and tidal coupling recovers.

A Conceptual model for tidal-sensitive sealing–rupture cycles

The temporal variation of observed tremor, microseismicity, and Vp/Vs maps onto a conceptual model of tide-regulated, valve-like behavior in the shallow oceanic transform fault zone (Fig. 5). This model unifies the co-evolution of fluid/gas supply, permeability, pore pressure, and tidal coupling gain into a repeatable, three-stage cycle.

Stage 1: Sealed and pressurized (Fig. 5B). With the shallow fracture network sealed, the continuous supply of magmatic volatiles (e.g., CO_2, as evidenced by the low Vp/Vs strip in Fig. 5A) and hydrothermal fluid from depth gradually elevates fault zone pore pressure. As the gas fraction increases, it drives a systematic decrease in Vp/Vs. As the resonance source approaches a near-critical state with near-lithostatic pore pressure, the tidal volume strain is sufficient to modulate tremor excitation and radiation intensity, producing tidally modulated harmonic tremor. Permeability further controls the hydraulic response time, leading to a phase lag between tidal forcing and tremor energy. During this stage, microseismicity is relatively low.

Stage 2: Rupture opens pathways (Fig. 5C). When the escalating pore pressure and differential stress exceed the strength of the sealed fractures, earthquake rupture occurs. This "valve-opening" event breaks seals and creates new cracks, increasing porosity and permeability. The porosity gain drives transient dilatancy strengthening and a local decrease in pore pressure. In parallel, Vp/Vs increases as compressible gas is expelled, and liquid reinfiltrates along the newly connected pathways, enabling rapid pore-pressure equilibration. The increase in permeability shortens the hydraulic response time and breaks down the sealed conditions needed to sustain pore-pressure retention, so tremor energy no longer tracks the tidal cycle, and the tremor–tide correlation collapses. Meanwhile, the M4 rupture and subsequent stress transfer trigger a transient swarm of microearthquakes.

Stage 3: Fluid infiltration and progressive sealing (Fig. 5D). Following a rupture that re-opens pathways, hydrothermal circulation promotes healing and mineral precipitation within the fracture network (*7*, *33*). This chemical–mechanical sealing reduces permeability, progressively lowering hydraulic connectivity and increasing pore pressure, typically accompanied by abundant small earthquakes. The system resets to Stage 1 as sealing isolates volatile-rich fluids and restores strong tidal coupling.

In this framework earthquake rupture in the presence of fluid acts primarily by increasing permeability and reconnecting fracture pathways. The observed breakdown in tremor-tide correlation thus marks a transient "valve-opening" event, in which enhanced hydraulic connectivity weakens tidal coupling (*37*, *40*). At the laboratory scale, short-period pore-pressure oscillations reproducibly increase the permeability of fractured rock, producing step-like gains followed by gradual recovery toward the pre-perturbation state. This behavior is consistent with reversible unclogging of fracture pathways and provides a mechanistic link between dynamic stressing and transient hydraulic opening (*41*).

Global implications

Our work recasts oceanic transform faults from conservative shear boundaries into active, tide-fluid-magma coupled systems. The observed self-sealing cycles demonstrate that the energy budget on oceanic transform faults is not solely a function of elastic strain accumulation/release but is also paced by the internal dynamics of volatile supply and permeability evolution modulated by periodic tidal loads and moderate earthquake ruptures. This paradigm is supported by growing global evidence of first-order magmatic control in transform domains. Two-stage crustal accretion, intra-transform spreading centers, and pervasive magmatism provide the sustained volatile flux and geometric pathways that enable cyclic sealing, pressurization, and drainage (*2*, *4*, *42*, *43*). Fault zone architecture, shaped by this magmatic–tectonic interplay, creates the necessary plumbing for the valve-like behavior.

We propose that the phenomenon of tremor–tide correlation and sealing–rupture cycles is not unique to Gofar but likely widespread, particularly in settings with high slip rate and high volatile flux (*44*), such as the Marie Celeste Fracture Zone offsetting the Central Indian Ridge (*45*), the Garrett transform fault with intra-transform volcanism (*46*), the Chain transform with a broad fluid-transporting fault zone (*47*), and other segments of the Quebrada-Discovery-Gofar system (*48*). Transform segments near ridge–transform intersections, areas with faster spreading rates, or regions influenced by mantle hotspots should exhibit more pronounced tremor–tide correlation and more frequent valve-like resets. This observed tremor–tide correlation is similar to tidal modulated tremors in subduction zones (*11*) and the deep San Andreas fault zone (*8*), and tidal modulation of slow slip in Cascadia (*49*), suggesting that analogous tide-sensitive behaviors may emerge in other tectonic settings when faults approach near-critical, fluid-pressurized conditions. The diagnostic fingerprints—synchronized transitions in tremor–tide correlation, microseismicity rate, and Vp/Vs—provide a template for identifying and quantifying these dynamic processes and potential hazard at oceanic transform faults.

Materials and Methods

Data RMS time series and tidal correlation calculation

We used continuous waveforms recorded on 33 three-component broadband OBS stations (Fig. 1B) around G3 for the period of 2020-08-01 to 2020-12-31, which is a subset of an OBS seismic experiment consisting of 94 stations deployed across the Gofar during 2019–2022 (Fig. 1A) (*25*). Data preprocessing followed standard procedures: we de-meaned and de-trended the traces, removed instrument responses using the network inventory, and converted the waveform amplitudes to ground velocities (in µm/s). For each selected station, we bandpass-filtered the continuous velocity waveforms to the 2-8 Hz frequency band and computed the root-mean-square (RMS) time series using a 60 s sliding window with a 30 s step. We computed amplitude spectra of the RMS time series with a Hanning-window periodogram, converted the frequencies to periods (hours), restricted the display to 10-30 h, and normalized by the peak amplitude (Fig. 3). To minimize contamination from local earthquakes, we masked time windows from 10 s before to 40 s after the earthquake origin time using our relocated earthquake catalog.

Following the tidal calculation framework described in (*29*), the total tidal volume strain in the study area includes three components: body tide (or solid Earth tide), regional ocean-mass loading, and direct loading from the overlying water column. Positive strain denotes dilatation.

We first used SPOTL (*50*) to calculate the horizontal strain components induced by body tide, ε_{xx}^{BT} and ε_{yy}^{BT}. This software assumes an elastic, spherical Earth and computes tidal strain directly from the positions of the Moon and Sun. Under the plane-stress assumption, the vertical strain was then recovered from the horizontal strain components as

$$\varepsilon_{zz}^{BT} = -\frac{\nu}{1-\nu}\left(\varepsilon_{xx}^{BT} + \varepsilon_{yy}^{BT}\right) \quad (1)$$

We used a Poisson's ratio ν of 0.23, corresponding to Vp = 5.4 km/s, Vs = 3.2 km/s , and ρ = 2800 kg/m^3 based on previous seismic tomography studies in this area (*5*). The volume strain associated with body tide was then calculated as

$$\varepsilon_{v}^{BT} = \varepsilon_{xx}^{BT} + \varepsilon_{yy}^{BT} + \varepsilon_{zz}^{BT} \quad (2)$$

For the ocean-tide contribution, we first predicted tidal height variations, $h(t)$, for the eight principal short-period tidal constituents (K1, K2, M2, N2, O1, P1, Q1, and S2) using the global ocean tide model EOT11a (*51*). We then separated the ocean-tide effect into two parts. The first is the elastic loading response caused by regional ocean-mass redistribution. For this component, we used SPOTL with mass-loading Green's functions to calculate the horizontal strain components, ε_{xx}^{BT} and ε_{yy}^{BT}, and again recovered the vertical strain under the plane-stress assumption as

$$\varepsilon_{zz}^{ML} = -\frac{\nu}{1-\nu}\left(\varepsilon_{xx}^{ML} + \varepsilon_{yy}^{ML}\right) \quad (3)$$

The corresponding volume strain from regional ocean-mass loading is

$$\varepsilon_{v}^{ML} = \varepsilon_{xx}^{ML} + \varepsilon_{yy}^{ML} + \varepsilon_{zz}^{ML} \quad (4)$$

The second part is the direct pressure loading produced by local changes in the overlying water column. The resulting vertical normal stress at the seafloor is given by

$$\sigma_{zz}^{WL} = -\rho_w g h \quad (5)$$

where ρ_w = 1030 kg/m^3 and g = 9.8 m/s^2. The negative sign indicates that an increase in water column height corresponds to a larger compressive stress. Under the uniaxial-strain assumption, the horizontal strains satisfy $\varepsilon_{xx}^{WL} = \varepsilon_{yy}^{WL} = 0$, and the vertical strain is

$$\varepsilon_{zz}^{WL} = \frac{(1+\nu)(1-2\nu)}{(1-\nu)E}\sigma_{zz}^{WL} \quad (6)$$

where E is Young's modulus. The volume strain contribution from direct water-column loading is therefore

$$\varepsilon_{v}^{WL} = \varepsilon_{zz}^{WL} \quad (7)$$

Finally, we summed the body-tide, regional ocean-mass loading, and direct water-column loading contributions at each time step to obtain the total tidal volume strain time series:

$$\varepsilon_{v}^{\text{total}}(t) = \varepsilon_{v}^{BT}(t) + \varepsilon_{v}^{ML}(t) + \varepsilon_{v}^{WL}(t) \quad (8)$$

We bandpass-filtered the total tidal strain around the semidiurnal band and computed its unwrapped instantaneous phase. We then interpolated the tidal series at each RMS sampling time. For each station, we computed the mean RMS waveform value in each 0.5° phase bin, which is combined to form the array-mean RMS amplitude curve. We fitted the array-mean curve with a sinusoidal curve to measure the phase lag from the difference in peaks with the range −180° to 180°. In addition, we quantified phase-folded similarity by computing the maximum Pearson correlation between the fitted sinusoidal curve and the M2 tidal curve over all circular phase shifts.

To assess the spatial correlation of tremor energy, we computed a pairwise correlation between stations with Welch's method (Hanning windows, 50% overlap) using a time segment length of 12.4 h to target the semidiurnal band. For each station pair, we calculated the average correlation over 2-8 Hz. For all stations, a $N \times N$ correlation matrix is formed with N the number of stations. The correlation matrices before and after 8 September 2020 show array-wide high correlation (CC > 0.4) before rupture and a breakdown after rupture (fig. S9).

Tremor source locationWe located tremor sources using the waveform migration-based method with a semblance imaging condition, which is well suited for continuous, narrowband tremor signals (*52*). We first constructed a 3D grid over the study area with 0.2 km spacing in all directions, and computed predicted travel times from each grid node to each station using the same shear-wave velocity model as (*5*). For each grid node, we time-shifted the station RMS time series (three-component) by the predicted travel times and stacked them to compute the semblance. Within each sliding window, we scanned the entire grid and took the node with the maximum semblance as the most likely source location.

We validated this waveform-migration method for 56 selected M3+ earthquakes. Earthquake waveforms were bandpass-filtered to 5-10 Hz and a 2 s sliding window with a 0.2 s step was used to scan the first 8 s after the origin time. To enable a direct comparison between waveform-based and arrival time-based locations, we used only the stations included in the tomoDD relocation. For one example earthquake, the semblance values from waveform-migration based location method are well focused around the tomoDD location (fig. S2). Overall, the waveform-based locations agree with the arrival-based tomoDD locations, with the mean difference of ~1.5 km (fig. S3). However, there is a systematic shift with waveform-based locations are more slightly distributed to the north and deeper, which is due to that waveform-based location method only uses S waves and it gives the centroid locations instead of the initiation locations from arrival-based location method.

For the tremor-tide correlation interval, we scanned the processed RMS time series using a 6 s window with a 6 s step. For each window, we retained the top 2% of grid nodes by brightness and obtained cumulative hit count and cumulative brightness distribution by stacking results over all windows (fig. S4). The dominant tremor sources are concentrated near the transform fault within ~4.5 km below the seafloor, slightly shallower than the earthquake distribution. To further evaluate the reliability of located tremor source zone, we constructed random noise series at the same set of stations and repeated the same analysis as described above. In the absence of coherent sources, there is no focused energy (fig. S4). We also used the 2-hour RMS time series in the tremor-tide correlation interval to locate its tremor source and the result is almost identical to that located by using all RMS time series (fig. S5), suggesting that tremor sources are stable and persistent during the tremor-tide correlation interval.

Seismic event detection for the OBS array data

We followed the deep-learning-based AI–PAL workflow (*53*) to detect and locate earthquakes. We used the continuous data from 2020-01-01 to 2020-12-31 to generate region-specific high-quality labels. PAL used an STA/LTA energy trigger with STA windows of 0.35/0.12/0.12 s (detection/P/S), LTA windows of 3/0.4/0.4 s, a trigger threshold of 12; an S-wave amplitude window of [1, 4] s; a minimum detection gap of 5 s; and a 5-25 Hz band-pass. Association required more than 18 stations, origin-time deviation less than 0.6 s, and P-phase residual less than 0.8 s; locations were obtained by grid search (0.01° lat/lon spacing with 10% lateral margin; depth 3.5-20 km with 1 km spacing) with mean Vp=5.9 km/s and Vp/Vs=1.85. Manual screening yielded slightly over 1,000 high-quality earthquakes for training (fig. S12A).

We then self-supervised a Self-Attention RNN (SAR/LoSAR) picker on these PAL labels (100 Hz sampling; three components; 10 s sliding windows with 4 s stride; 128 hidden units; 3 layers; 0.2 s step with 0.04 s stride; 1,000 epochs; batch size 128). The trained model was applied to the continuous data from 2020-08-01 to 2020-10-01 and from 2020-10-01 to 2020-12-31, using a per-phase probability threshold 0.9; association by the PAL required more than 6 stations with origin-time deviation less than 0.6 s and P-residual less than 0.8 s. In total, we obtained 24,126 and 34,594 events for two time periods, respectively, forming a high-quality earthquake catalog (fig. S12B).

Earthquake relocation by the double-difference location method

We first used the HYPOINVERSE method (*54*) to obtain absolute locations. The HYPOINVERSE method iteratively minimizes travel-time residuals, with phase weights adaptively set by epicentral distance and residual. The 1D P-wave velocity profile was extracted from a 3D P-wave velocity model (*5*); the corresponding 1D S-wave velocity model was derived by assuming Vp/Vs = 1.9 in the crust and Vp/Vs = 1.8 in the mantle with the Moho depth at 6.85 km.

We then refined the HYPOINVERSE locations with tomoDD (*55*). tomoDD jointly inverts velocity structure and event locations using both absolute and relative arrival times, which is an extension of the double-difference location method (*56*). Here we fixed the velocity model and solved for locations using the high-resolution 3D velocity structure constructed for the Gofar G3 segment (*5*). We first removed outliers based on traveltime-distance curve, and constructed event-pair differential arrival times. Waveform cross correlation was also used to calculate more accurate differential arrival times. We started from the HYPOINVERSE locations, and relocated events using the three types of travel times by the tomoDD with the 3D velocity model fixed. A two-stage strategy was adopted: (i) optimize absolute locations by having higher weights on absolute travel times; (ii) increase the weights on differential catalog arrival times and cross-correlation times to sharpen relative event locations. Events spuriously located in the water were removed using seafloor bathymetry. In total, we obtained 20,426 events for the period of 2020-08-01 to 2020-10-01, with the final RMS travel time residual of 11.1 ms for waveform cross-correlation times, and 29,741 events for the period of 2020-10-01 to 2020-12-31, with the final RMS travel time residual of 9.7 ms for waveform cross-correlation times.

In-situ Vp/Vs estimation
We followed the method of (*57*) for the in-situ Vp/Vs estimation. We defined five spatial anchors A0-A4 (fig. S13) and around each anchor we expanded a 3-D neighborhood until we collected the 80-90 earthquakes for in-situ Vp/Vs estimation. For the selected events around each anchor, we built high-quality P and S differential travel times for event pairs. For each event pair (i, j) and station k, we measured differential P and S arrival times $\Delta t_P(k;i,j)$ and $\Delta t_S(k;i,j)$ using waveform cross correlation, and retained measurements with waveform cross-correlation coefficient $cc \geq 0.7$. For each pair, Δt_P and Δt_S were then demeaned across stations (subtracting the station-mean for that pair) to remove pair-specific timing offsets and common terms. The resulting demeaned differentials from all qualified pairs at a given anchor were pooled for Vp/Vs estimation. Outliers were suppressed with a density filter in the ($\Delta t_P, \Delta t_S$) domain (DBSCAN, eps ≈ 0.03 s, min_samples ≈ 20).

We estimated Vp/Vs by fitting (*57*),

$$\Delta t_S = a + b\Delta t_P \quad (9)$$

using robust least squares inversion with multi-round 2σ clipping. In practice, we repeatedly linear fit by minimizing orthogonal misfit and removing points with orthogonal residuals $> 2\sigma$; the final slope b is taken as in-situ Vp/Vs for the event cluster around each anchor. We computed a 95% confidence interval (CI) for b by performing an orthogonal distance regression (ODR) on the final line and using the ODR slope standard error $\mathrm{SE}_{\hat{b}}$:

$$\hat{b} \pm t_{0.975,n-2}\mathrm{SE}_{\hat{b}} \quad (10)$$

Repeating this procedure through time intervals yields the Vp/Vs series in Fig. 4B.

Estimation of pore pressure response to tidal forcing
Following (*35*), pore-pressure evolution in a poroelastic medium satisfies

$$S_\epsilon \frac{\partial p}{\partial t} + \nabla \cdot \boldsymbol{q} = -\alpha \frac{\partial \varepsilon_v}{\partial t} \quad (11)$$

with Darcy flux $\mathbf{q} = -\frac{k}{\mu}\nabla(p - p_0)$ Here p is pore pressure, ε_v is volumstrain, $\alpha = 1 - K/K_s$ is the Biot coefficient with K drained-frame bulk modulus and K_s solid bulk modulus; $S_\epsilon = \alpha^2/(K_u - K)$ is the constrained storage compressibility with K_u undrained bulk modulus, *k* is permeability, μ is dynamic viscosity, and p_0 is hydrostatic pressure.

Integrating Eq. 11 over a representative volume V and applying the divergence theorem yields,

$$S_\epsilon \frac{d\overline{p}}{dt} + \frac{1}{V}\oint_{\partial V} \mathbf{q}\cdot\mathbf{n}dA = -\alpha \frac{d\overline{\varepsilon}_v}{dt} \quad (12)$$

where overbars denote volume averages and $\mathbf{n}$ is the outward normal. We parameterize net drainage to an external reservoir at pressure p_0 by a thin-layer Darcy approximation across a characteristic length ℓ:

$$\frac{1}{V}\oint_{\partial V} \mathbf{q}\cdot\mathbf{n}dA \approx -\frac{k}{\mu}\frac{A}{V\ell}(p_0 - \overline{p}) \equiv \frac{k}{\mu\nu}(\overline{p} - p_0) \quad (13)$$

where A is the effective draining area and $\nu \equiv V\ell / A$ absorbs geometry.

Substituting into Eq. 12 gives

$$S_\epsilon \frac{d\overline{p}}{dt} + \frac{k}{\mu\nu}(\overline{p} - p_0) = -\alpha \frac{d\overline{\varepsilon}_v}{dt} \, S_\epsilon \simeq \phi C_w \quad (14)$$

Decompose $\overline{p}(t) = p_0 + p'(t)$ and $\overline{\varepsilon}_v(t) = \varepsilon_0 + \varepsilon'_v(t)$. Eq. 14 becomes

$$\frac{dp'}{dt} + \frac{k}{S_\epsilon \mu\nu}p' = -\frac{\alpha}{S_\epsilon}\frac{d\varepsilon'_v}{dt} \quad (15)$$

Finally, under the approximations of a nearly incompressible frame such that constrained storage is fluid-dominated, (with $C_w \equiv 1/K_f$ the fluid compressibility, ϕ is porosity), $\alpha \simeq 1$, then,

$$\frac{dp'}{dt} + \frac{1}{\tau}p' = -\frac{1}{\phi C_w}\frac{d\varepsilon'_v}{dt}, \quad \tau = \frac{\phi C_w \mu\nu}{k} \quad (16)$$

The parameter τ is the characteristic diffusion timescale for pore-pressure equilibration, which governs the amplitude of the response to periodic volume strain loading and the associated phase lag for a given permeability and storage capacity.

We use the predicted total tidal volume strain $\varepsilon_v^{\mathrm{total}}(t)$ as the external loading. We define $\phi(t) = \phi_0 + \phi'(t)$, where ϕ_0 is the background porosity set to be 0.03 and $\phi'(t)$ is the tidal porosity perturbation converted from volume strain using the Biot coefficient. For simplicity we take α = 1.0. Fluid properties are prescribed as a dynamic viscosity $\mu = 1.0\times10^{-3}$ Pa s and a high pressure water compressibility $C_w = 2.0\times10^{-10}$ Pa^{-1}. The geometric factor ν is set to 1 due to limited constraints, which mainly affects the absolute response amplitude and timescale but not the relative trends associated with the evolution of permeability $k(t)$. These parameter ranges refer to previous studies of the Gofar transform fault (*21*).

To represent transient permeability enhancement by rupture and subsequent sealing/healing, we prescribe a time-dependent permeability $k(t)$ that increases rapidly around E2 on 8 September 2020 (within 1 day) from $k_{\mathrm{pre}} = 3.5\times10^{-19}$ m^2 to $k_{\mathrm{peak}} = 2.0\times10^{-16}$ m^2, followed by an exponential recovery toward the pre-event level, reaching a remaining fraction of 10^{-5} by the end of the modeled interval (fig. S18A). Results in Figure S18 show that during the tremor-tide correlation window, the pore pressure traces the M2 tidal signals with a cross-correlation coefficient of 0.97 and phase lag of -21°, consistent with the observed phase lag of -21° (Fig. 3B). Because pore pressure responds through diffusion, it does not follow volume strain instantaneously. As the volume strain rate decreases, the response becomes more drainage-dominated and pore pressure recovers earlier, so pore pressure leads volume strain, producing a phase lag of -90° to 0° that is controlled by a characteristic diffusion timescale (τ); in contrast, the pore pressure response to the tidal loading is extremely low during the decorrelation interval because of the high permeability.

REFERENCES AND NOTES

1. J. T. Wilson, A new class of faults and their bearing on continental drift. *Nature* **207**, 343–347 (1965). doi:10.1038/207343a0
2. W. R. Buck, L. L. Lavier, A. N. B. Poliakov, Modes of faulting at mid-ocean ridges. *Nature* **434**, 719–723 (2005). doi:10.1038/nature03358 Medline
3. P. M. Gregg, J. Lin, M. D. Behn, L. G. J. Montési, Spreading rate dependence of gravity anomalies along oceanic transform faults. *Nature* **448**, 183–187 (2007). doi:10.1038/nature05962 Medline
4. I. Grevemeyer, L. H. Rüpke, J. P. Morgan, K. Iyer, C. W. Devey, Extensional tectonics and two-stage crustal accretion at oceanic transform faults. *Nature* **591**, 402–407 (2021). doi:10.1038/s41586-021-03278-9 Medline
5. H. Guo, H. Zhang, B. Froment, Structural control on earthquake behaviors revealed by high-resolution Vp/Vs imaging along the Gofar transform fault, East Pacific Rise. *Earth Planet. Sci. Lett.* **499**, 243–255 (2018). doi:10.1016/j.epsl.2018.07.037
6. M. F. H. Thomas, C. Heine, J. Van Itterbeeck, I. Ostanin, A. Seregin, M. Spaak, T. Morales, T. O. Essink, A new model for the evolution of oceanic transform faults based on 3D broadband seismic observations from São Tomé and Príncipe in the eastern Gulf of Guinea. *Geochem. Geophys. Geosyst.* **23**, e2022GC010351 (2022). doi:10.1029/2022GC010351
7. R. H. Sibson, Implications of fault-valve behaviour for rupture nucleation and recurrence. *Tectonophysics* **211**, 283–293 (1992). doi:10.1016/0040-1951(92)90065-E
8. A. M. Thomas, R. M. Nadeau, R. Bürgmann, Tremor-tide correlations and near-lithostatic pore pressure on the deep San Andreas fault. *Nature* **462**, 1048–1051 (2009). doi:10.1038/nature08654 Medline
9. B. A. Chouet, Long-period volcano seismicity: Its source and use in eruption forecasting. *Nature* **380**, 309–316 (1996). doi:10.1038/380309a0
10. K. Obara, Nonvolcanic deep tremor associated with subduction in southwest Japan. *Science* **296**, 1679–1681 (2002). doi:10.1126/science.1070378 Medline
11. J. L. Rubinstein, M. La Rocca, J. E. Vidale, K. C. Creager, A. G. Wech, Tidal modulation of nonvolcanic tremor. *Science* **319**, 186–189 (2008). doi:10.1126/science.1150558 Medline
12. R. P. Dziak, J. H. Haxel, H. Matsumoto, T. K. Lau, S. G. Merle, C. E. J. De Ronde, R. W. Embley, D. K. Mellinger, Observations of regional seismicity and local harmonic tremor at Brothers Volcano, South Kermadec Arc, using an ocean bottom hydrophone array. *J. Geophys. Res.* **113** (B8), 2007JB005533 (2008). doi:10.1029/2007JB005533
13. R. P. Dziak, C. G. Fox, Evidence of harmonic tremor from a submarine volcano detected across the Pacific Ocean basin. *J. Geophys. Res.* **107** (B5), ESE 1-1, 1–11 (2002). doi:10.1029/2001JB000177
14. P. W. Monigle, D. R. Bohnenstiehl, M. Tolstoy, F. Waldhauser, Seismic tremor at the 9°50′N East Pacific Rise eruption site. *Geochem. Geophys. Geosyst.* **10**, 2009GC002561 (2009). doi:10.1029/2009GC002561
15. M. Tolstoy, F. L. Vernon, J. A. Orcutt, F. K. Wyatt, Breathing of the seafloor: Tidal correlations of seismicity at Axial Volcano. *Geology* **30**, 503–507 (2002). doi:10.1130/0091-7613(2002)030<0503:BOTSTC>2.0.CO;2
16. J. J. McGuire, M. S. Boettcher, T. H. Jordan, Foreshock sequences and short-term earthquake predictability on East Pacific Rise transform faults. *Nature* **434**, 457–461 (2005). doi:10.1038/nature03377 Medline
17. B. Froment, J. J. McGuire, R. D. Van Der Hilst, P. Gouédard, E. C. Roland, H. Zhang, J. A. Collins, Imaging along-strike variations in mechanical properties of the Gofar transform fault, East Pacific Rise. *J. Geophys. Res. Solid Earth* **119**, 7175–7194 (2014). doi:10.1002/2014JB011270
18. E. Roland, D. Lizarralde, J. J. McGuire, J. A. Collins, eismic velocity constraints on the material properties that control earthquake behavior at the Quebrada-Discovery-Gofar transform faults, East Pacific Rise. *J. Geophys. Res.* **117** (B11), 2012JB009422 (2012). doi:10.1029/2012JB009422
19. J. Gong, W. Fan, Seismicity, fault architecture, and slip mode of the westernmost Gofar transform fault. *J. Geophys. Res. Solid Earth* **127**, e2022JB024918 (2022). doi:10.1029/2022JB024918
20. J. Gong, W. Fan, R. Parnell-Turner, Machine learning-based new earthquake catalog illuminates on-fault and off-fault seismicity patterns at the Discovery transform fault, East Pacific Rise. *Geochem. Geophys. Geosyst.* **24**, e2023GC011043 (2023). doi:10.1029/2023GC011043
21. Y. Liu, J. J. McGuire, M. D. Behn, Aseismic transient slip on the Gofar transform fault, East Pacific Rise. *Proc. Natl. Acad. Sci. U.S.A.* **117**, 10188–10194 (2020). doi:10.1073/pnas.1913625117 Medline
22. J. J. McGuire, J. A. Collins, P. Gouédard, E. Roland, D. Lizarralde, M. S. Boettcher, M. D. Behn, R. D. Van Der Hilst, Variations in earthquake rupture properties along the Gofar transform fault, East Pacific Rise. *Nat. Geosci.* **5**, 336–341 (2012). doi:10.1038/ngeo1454
23. P. A. Moyer, M. S. Boettcher, J. J. McGuire, J. A. Collins, Spatial and temporal variations in earthquake stress drop on Gofar transform fault, East Pacific Rise: Implications for fault strength. *J. Geophys. Res. Solid Earth* **123**, 7722–7740 (2018). doi:10.1029/2018JB015942
24. C. Chesley, R. Evans, J. M. Warren, A. C. Gase, J. Perez, C. Armerding, H. Brewer, P. Koenig, E. Attias, B. L. Fluegel, J.-D. Kim, N. Hummel, K. Enright, E. Topp-Johnson, M. S. Boettcher, Evidence for crustal brines and deep fluid infiltration in an oceanic transform fault. *Sci. Adv.* **11**, eadu3661 (2025). doi:10.1126/sciadv.adu3661 Medline
25. M. Boettcher, M. Behn, W. Fan, J. Warren, J. McGuire, J. Collins, E. Roland, Y. Liu, 8A (2019-2022): Gofar_Transfrom_Fault (International Federation of Digital Seismograph Networks, 2019); https://doi.org/10.7914/SN/8A_2019.
26. B. R. Julian, Volcanic tremor: Nonlinear excitation by fluid flow. *J. Geophys. Res.* **99** (B6), 11859–11877 (1994). doi:10.1029/93JB03129
27. A. Ghosh, J. E. Vidale, K. C. Creager, Tremor asperities in the transition zone control evolution of slow earthquakes. *J. Geophys. Res.* **117** (B10), 2012JB009249 (2012). doi:10.1029/2012JB009249
28. A. Ghosh, J. E. Vidale, J. R. Sweet, K. C. Creager, A. G. Wech, H. Houston, Tremor bands sweep Cascadia. *Geophys. Res. Lett.* **37**, 2009GL042301 (2010). doi:10.1029/2009GL042301
29. Y. J. Tan, F. Waldhauser, M. Tolstoy, W. S. D. Wilcock, Axial Seamount: Periodic tidal loading reveals stress dependence of the earthquake size distribution (b value). *Earth Planet. Sci. Lett.* **512**, 39–45 (2019). doi:10.1016/j.epsl.2019.01.047
30. D. H. Johnston, M. N. Toksoz, A. Timur, Attenuation of seismic waves in dry and saturated rocks; II, mechanisms. *Geophysics* **44**, 691–711 (1979). doi:10.1190/1.1440970
31. M. N. Toksoz, C. H. Cheng, A. Timur, Velocities of seismic waves in porous rocks. *Geophysics* **41**, 621–645 (1976). doi:10.1190/1.1440639
32. Y. Liu, J. M. Kendall, H. Zhang, J. D. Blundy, M. E. Pritchard, T. Hudson, P. MacQueen, Anatomy of the magmatic-hydrothermal system beneath Uturuncu volcano, Bolivia, by joint seismological and petrophysical analysis. *Proc. Natl. Acad. Sci. U.S.A.* **122**, e2420996122 (2025). doi:10.1073/pnas.2420996122 Medline
33. H. Yasuhara, D. Elsworth, A. Polak, Evolution of permeability in a natural fracture: Significant role of pressure solution. *J. Geophys. Res.* **109** (B3), 2003JB002663 (2004). doi:10.1029/2003JB002663
34. H. Yu, R. M. Harrington, H. Kao, Y. Liu, B. Wang, Fluid-injection-induced earthquakes characterized by hybrid-frequency waveforms manifest the transition from aseismic to seismic slip. *Nat. Commun.* **12**, 6862 (2021).

doi:10.1038/s41467-021-26961-x Medline
35. T. J. Crone, W. S. D. Wilcock, Modeling the effects of tidal loading on mid-ocean ridge hydrothermal systems. *Geochem. Geophys. Geosyst.* **6**, 2004GC000905 (2005). doi:10.1029/2004GC000905
36. L. Jiang, S. Zhang, X. Li, Hydro-mechanical controls on swarm recurrence on the westernmost Gofar transform fault, East Pacific Rise. *Geophys. Res. Lett.* **53**, e2025GL119319 (2026). doi:10.1029/2025GL119319
37. L. Xue, H.-B. Li, E. E. Brodsky, Z.-Q. Xu, Y. Kano, H. Wang, J. J. Mori, J.-L. Si, J.-L. Pei, W. Zhang, G. Yang, Z.-M. Sun, Y. Huang, Continuous permeability measurements record healing inside the Wenchuan earthquake fault zone. *Science* **340**, 1555–1559 (2013). doi:10.1126/science.1237237 Medline
38. D. E. Moore, D. A. Lockner, J. D. Byerlee, Reduction of permeability in granite at elevated temperatures. *Science* **265**, 1558–1561 (1994). doi:10.1126/science.265.5178.1558 Medline
39. S. Ide, Striations, duration, migration and tidal response in deep tremor. *Nature* **466**, 356–359 (2010). doi:10.1038/nature09251 Medline
40. J. E. Elkhoury, E. E. Brodsky, D. C. Agnew, Seismic waves increase permeability. *Nature* **441**, 1135–1138 (2006). doi:10.1038/nature04798 Medline
41. J. E. Elkhoury, A. Niemeijer, E. E. Brodsky, C. Marone, Laboratory observations of permeability enhancement by fluid pressure oscillation of in situ fractured rock. *J. Geophys. Res. Solid Earth* **116**, B02311 (2011).
42. J.-A. Olive, G. Ekström, W. R. Buck, Z. Liu, J. Escartín, M. Bickert, Mid-ocean ridge unfaulting revealed by magmatic intrusions. *Nature* **628**, 782–787 (2024). doi:10.1038/s41586-024-07247-w Medline
43. X. Tian, M. D. Behn, G. Ito, J. C. Schierjott, B. J. P. Kaus, A. A. Popov, Magmatism controls global oceanic transform fault topography. *Nat. Commun.* **15**, 1914 (2024). doi:10.1038/s41467-024-46197-9 Medline
44. P. Shi, M. M. Wei, R. A. Pockalny, M. (Matt) Wei, R. A. Pockalny, The ubiquitous creeping segments on oceanic transform faults. *Geology* **50**, 199–204 (2022). doi:10.1130/G49562.1
45. B. J. Murton, A. G. Tindle, J. A. Milton, D. Sauter, Heterogeneity in Southern Central Indian Ridge MORB: Implications for ridge–hot spot interaction. *Geochem. Geophys. Geosyst.* **6**, 2004GC000798 (2005). doi:10.1029/2004GC000798
46. R. Hékinian, D. Bideau, R. Hébert, Y. Niu, Magmatism in the Garrett transform fault (East Pacific Rise near 13°27′S). *J. Geophys. Res.* **100** (B6), 10163–10185 (1995). doi:10.1029/94JB02125
47. K. Leptokaropoulos, C. A. Rychert, N. Harmon, D. Schlaphorst, I. Grevemeyer, J.-M. Kendall, S. C. Singh, Broad fault zones enable deep fluid transport and limit earthquake magnitudes. *Nat. Commun.* **14**, 5748 (2023). doi:10.1038/s41467-023-41403-6 Medline
48. R. C. Pickle, D. W. Forsyth, N. Harmon, A. N. Nagle, A. Saal, Thermo-mechanical control of axial topography of intra-transform spreading centers. *Earth Planet. Sci. Lett.* **284**, 343–351 (2009). doi:10.1016/j.epsl.2009.05.004
49. J. C. Hawthorne, A. M. Rubin, Tidal modulation of slow slip in Cascadia. *J. Geophys. Res.* **115** (B9), 2010JB007502 (2010). doi:10.1029/2010JB007502
50. D. C. Agnew, NLOADF: A program for computing ocean-tide loading. *J. Geophys. Res.* **102** (B3), 5109–5110 (1997). doi:10.1029/96JB03458
51. R. Savcenko, W. Bosch, EOT11a-empirical ocean tide model from multi-mission satellite altimetry, DGFI Report No. 89 (2012).
52. S. Miao, G. Cheng, H. Zhang, Y. Huang, N. Gu, H. Zha, J. Gao, Efficiently identifying coalbed methane enrichment areas by detecting and locating low-frequency signals in the coal mine. *Geohaz. Mech.* **1**, 86–93 (2023). doi:10.1016/j.ghm.2022.12.003
53. Y. Zhou, H. Ding, A. Ghosh, Z. Ge, AI-PAL: Self-supervised AI phase picking via rule-based algorithm for generalized earthquake detection. *J. Geophys. Res. Solid Earth* **130**, e2025JB031294 (2025). doi:10.1029/2025JB031294
54. F. W. Klein, User's guide to HYPOINVERSE-2000, a Fortran program to solve for earthquake locations and magnitudes (US Geological Survey, 2002).
55. H. Zhang, C. H. Thurber, Double-difference tomography: The method and its application to the Hayward Fault, California. *Bull. Seismol. Soc. Am.* **93**, 1875–1889 (2003). doi:10.1785/0120020190
56. F. Waldhauser, A double-difference earthquake location algorithm: Method and application to the northern Hayward Fault, California. *Bull. Seismol. Soc. Am.* **90**, 1353–1368 (2000). doi:10.1785/0120000006
57. G. Lin, P. M. Shearer, Evidence for water-filled cracks in earthquake source regions. *Geophys. Res. Lett.* **36**, 2009GL039098 (2009). doi:10.1029/2009GL039098
58. H. Yang, L. Ye, H. Zhang, Data and code for "Cyclic sealing and drainage on an oceanic transform fault", Zenodo (2026); https://doi.org/10.5281/zenodo.19871387.
59. A. M. Dziewonski, T.-A. Chou, J. H. Woodhouse, Determination of earthquake source parameters from waveform data for studies of global and regional seismicity. *J. Geophys. Res.* **86** (B4), 2825–2852 (1981). doi:10.1029/JB086iB04p02825
60. G. Ekström, M. Nettles, A. M. Dziewonski, The global CMT project 2004-2010: Centroid-moment tensors for 13,017 earthquakes. *Phys. Earth Planet. Inter.* **200-201**, 1–9 (2012). doi:10.1016/j.pepi.2012.04.002

ACKNOWLEDGMENTS

We are grateful for constructive comments from two anonymous reviewers. We thank Y. J. Tan with the discussion on the oceanic tidal calculation and the team (M. Boettcher, M. Behn, W. Fan, J. Warren, J. McGuire, J. Collins, E. Roland, and Y. Liu) who made the Gofar transform fault OBS data publicly available. **Funding:** This work was supported by the National Key Research and Development Program of China under grant no. 2022YFF0800700 (H.Z.) and the National Natural Science Foundation of China under grant no. 42488301 (H.Y.). **Author contributions:** Supervision: H.Z.; Conceptualization: H.Z., H.Y., L.Y.; Methodology: H.Y., H.Z.; Investigation: H.Y., H.Z.; Visualization: H.Y.; Writing – original draft: H.Y., H.Z.; Writing – review & editing: H.Z., L.Y., H.Y. **Competing interests:** The authors declare that they have no competing interests. **Data, code, and materials availability:** The waveform data used in this study can be accessed through the IRIS Data Management Center (*25*). Earthquake locations and necessary codes used in this study are available at Zenodo (*58*). All other data needed to evaluate the conclusions in the paper are included in the paper or the supplementary materials. No new samples or physical materials were collected or generated for this study.

SUPPLEMENTARY MATERIALS

science.sciencemag.org/cgi/content/full/science.aed5665/DC1
Figures S1 to S18

Submitted 01 November 2025; accepted 04 May 2026
Published online 25 June 2026
10.1126/science.aed5665

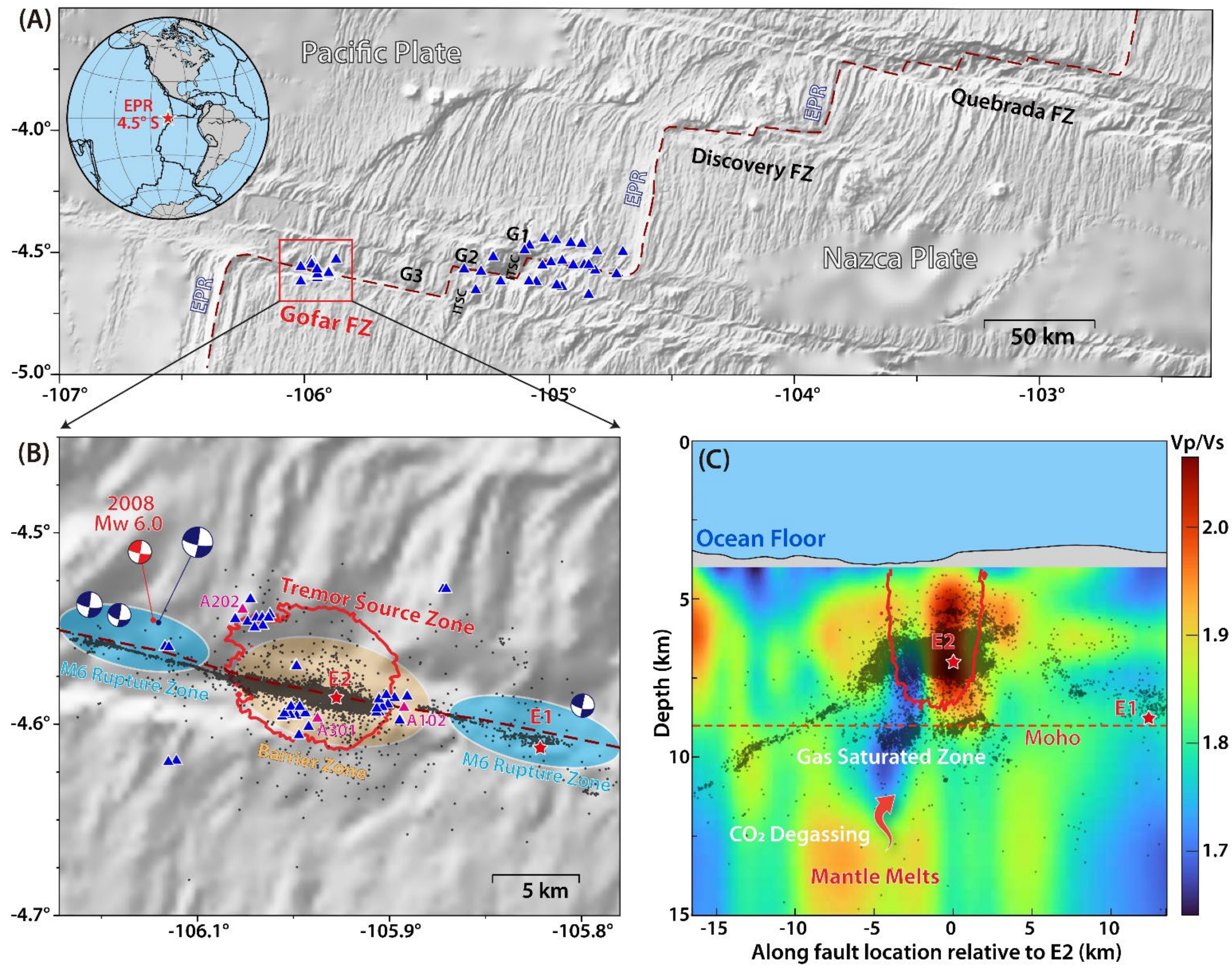

Fig. 1. Tectonic setting and seismicity of the Gofar transform fault. (**A**) Map view of the East Pacific Rise (EPR) mid-ocean ridge and transform system, with the Gofar (sections G1, G2, G3), Discovery, and Quebrada fracture zones (FZ) taking up transform slip between EPR spreading centers. Blue triangles denote ocean-bottom seismometers deployed from 2019–2022. Inset shows the regional plate boundary context. (**B**) Close-up of the study area on the Gofar transform fault (G3). Focal mechanisms show historical Mw ≥ 6.0 events from the Global Centroid Moment Tensor catalog (https://www.globalcmt.org/) (*59*, *60*). Cyan and yellow ellipses show the M6 earthquake ruptures and barrier zone, respectively (*22*). Black dots are relocated earthquakes from this study. The red contour outlines the region enclosing the top 25% of tremor energy. (**C**) Depth (below sea surface) profile of seismicity along the G3 segment relative to the location of the 8 September 2020, M4.0 earthquake (E2). The 11 August 2020 M4.1 earthquake (E1) is also marked. The profile defines three distinct domains: a shallow hydrothermal zone (seafloor to ~5 km), an intermediate brittle regime (~5-9 km), and a deeper magmatic-volatile domain (>9 km) rich in CO_2, as evidenced by low Vp/Vs anomalies. The red dashed line indicates the approximate Moho depth. The Vp/Vs model is from ref. (*5*).

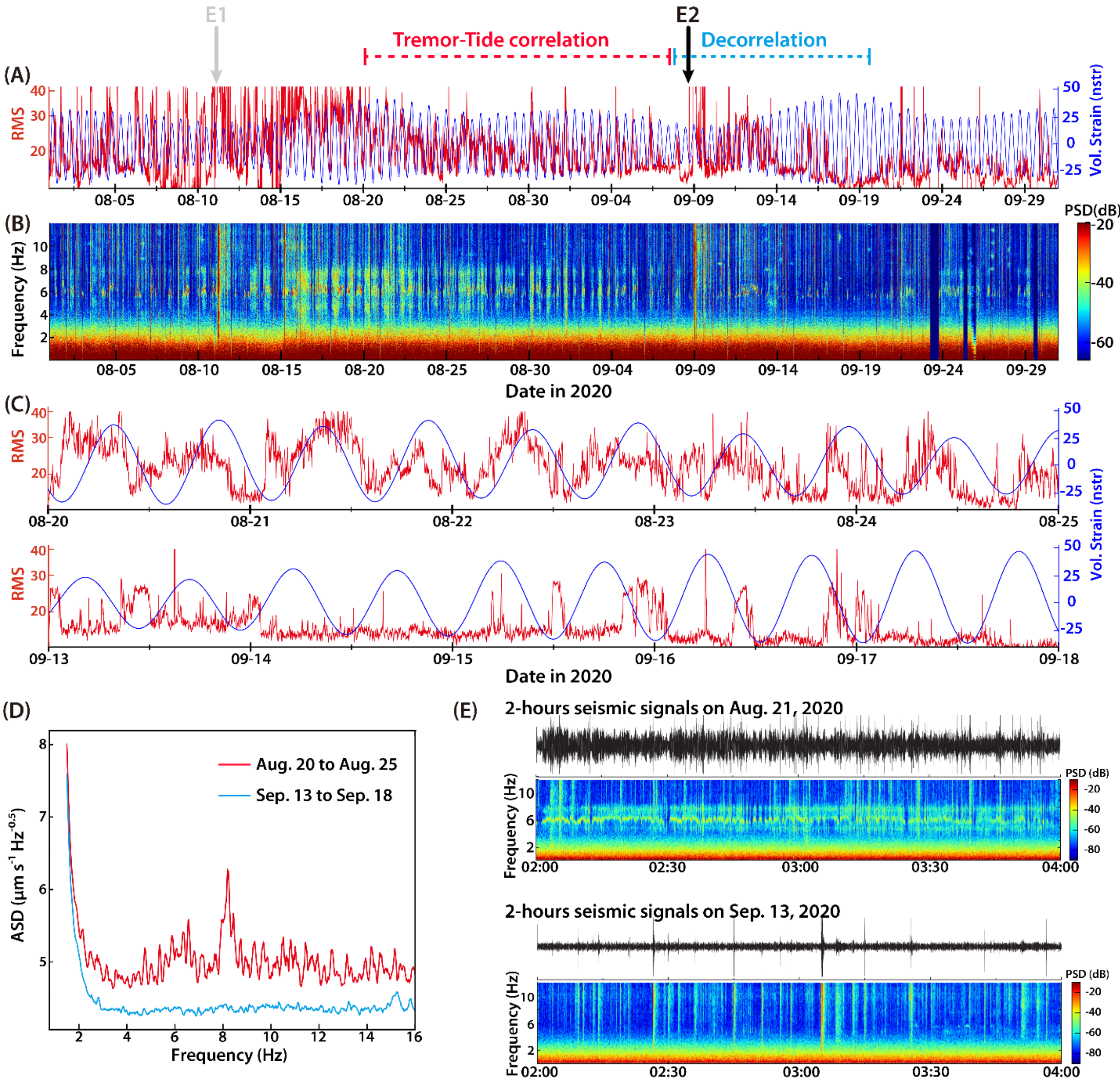

Fig. 2. Semidiurnal tidal modulation of tremor energy and its post-mainshock loss of correlation. (**A**) Root-mean-square (RMS) velocity amplitude at station A301 (2-8 Hz; red) from 2020-08-01 to 2020-10-01, overlaid with the total tidal volume strain (blue; extension positive). The gray and black vertical lines mark the 2020-08-11 M4.1 (E1) and 2020-09-08 M4.0 event (E2) earthquakes, respectively. (**B**) Power spectral density (PSD) spectrogram, highlighting persistent narrow-band harmonic tremor energy at 2-8 Hz from August 20 to early September. (**C**) 5-day zooms for the correlation window from August 20 to 25 and the decorrelation window from September 13 to 18, illustrating the transition from clear tidal modulation to the breakdown of correlation after the E2 mainshock. (**D**) Amplitude spectral densities (ASD) computed for the time windows in (C) after removing earthquake signals. (**E**) Two-hour raw seismic waveform and spectrogram on August 21 and September 13, respectively.

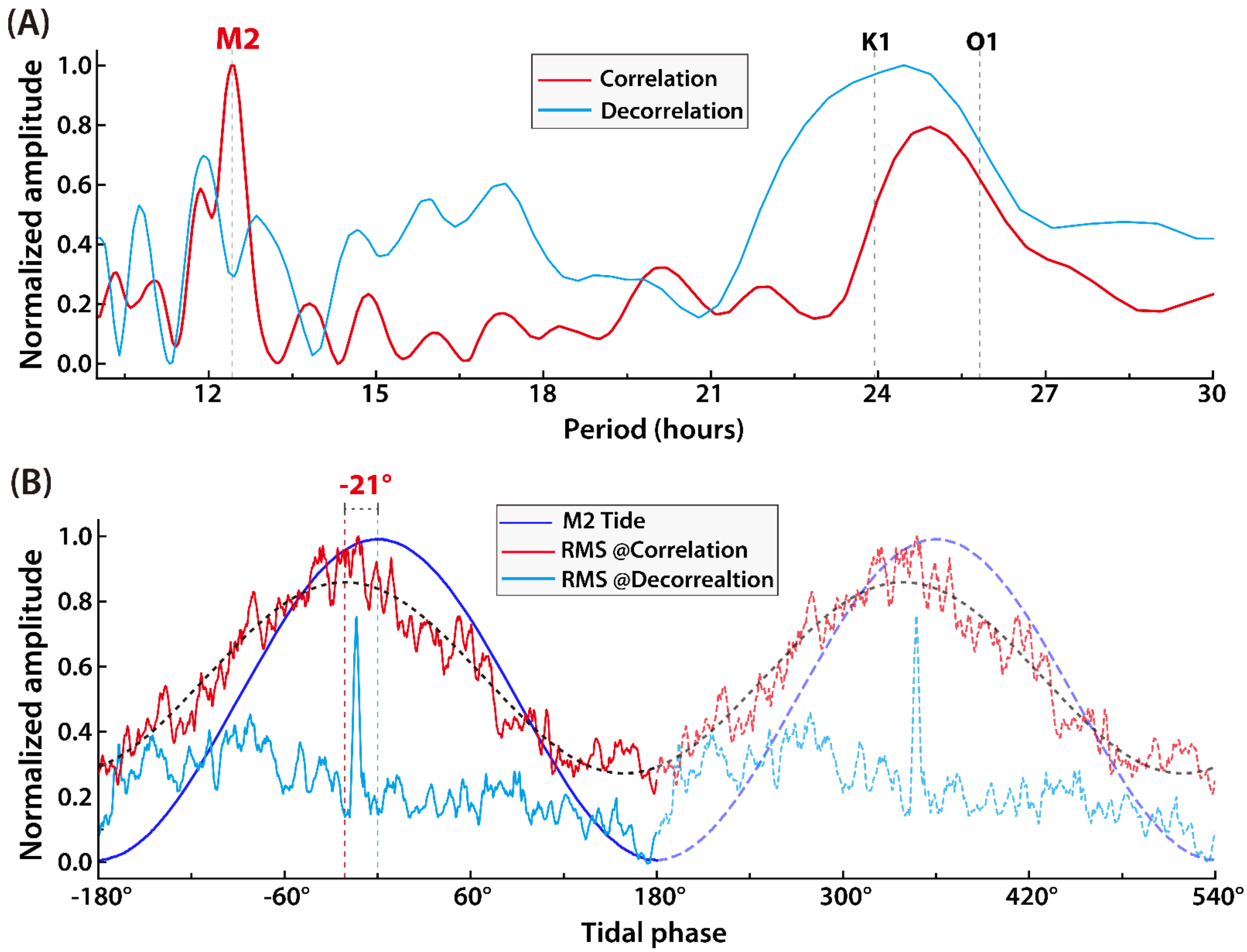

Fig. 3. Tidal correlation and breakup before and after the M4 rupture (E2). (**A**) Mean periodogram of vertical RMS averaged over all stations for the correlation (red) and decorrelation (cyan) windows (defined in Fig. 2). Dashed lines mark the tidal constituents M2 (12.4 hours), K1 (23.9 hours), and O1 (25.8 hours). (**B**) Phase-folded mean RMS across all available stations relative to the M2 tide, with tremor-tide cross-correlation coefficients 0.92 and 0.44 for correlation and decorrelation windows, respectively. The dashed black curve shows sinusoidal fit for the correlation interval. During this interval, the tremor energy (red) follows the M2 tide with a phase lag of -21.0°.

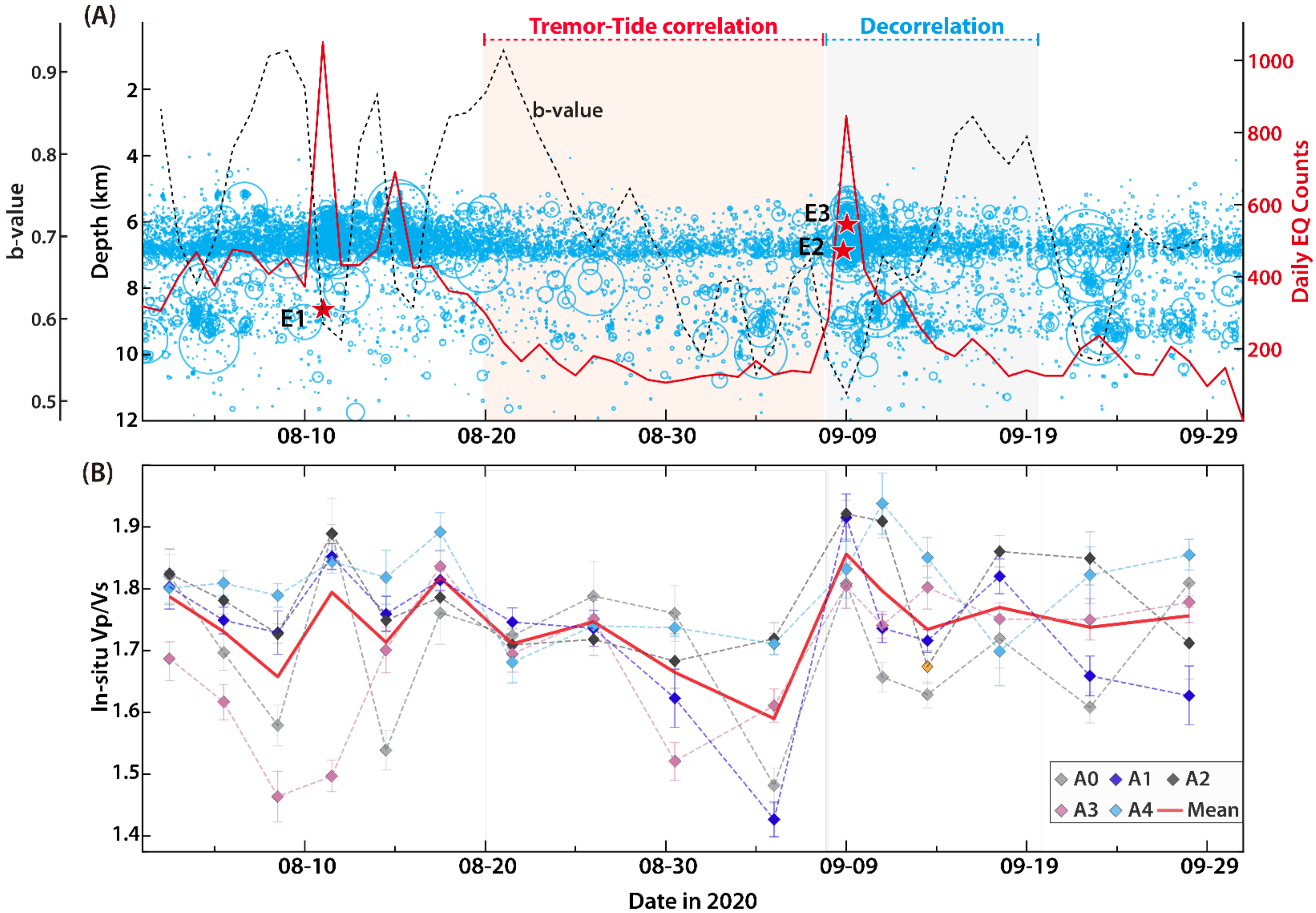

Fig. 4. Co-evolution of seismicity and fault-zone properties. (**A**) Temporal variation of relocated earthquakes. Circle size scales with earthquake magnitude. Three M4.0+ earthquakes (E1-E3) are highlighted by red stars. The red curve shows daily seismicity rate, and the dashed magenta curve shows the temporal evolution of the b-value. Only events above the completeness magnitude (Mc=0.3) are plotted and used to compute the seismicity rate and b-value. (**B**) Temporal variations in in-situ Vp/Vs at 5 fixed spatial anchors (A0-A4). Error bars indicate the 95% confidence intervals of the Vp/Vs estimates, and each marker is plotted at the center of its estimation window. The thick red curve is the average Vp/Vs value from 5 anchors. Details of anchor locations, time window and data fitting are shown in the supplementary materials (figs. S13 and S14).

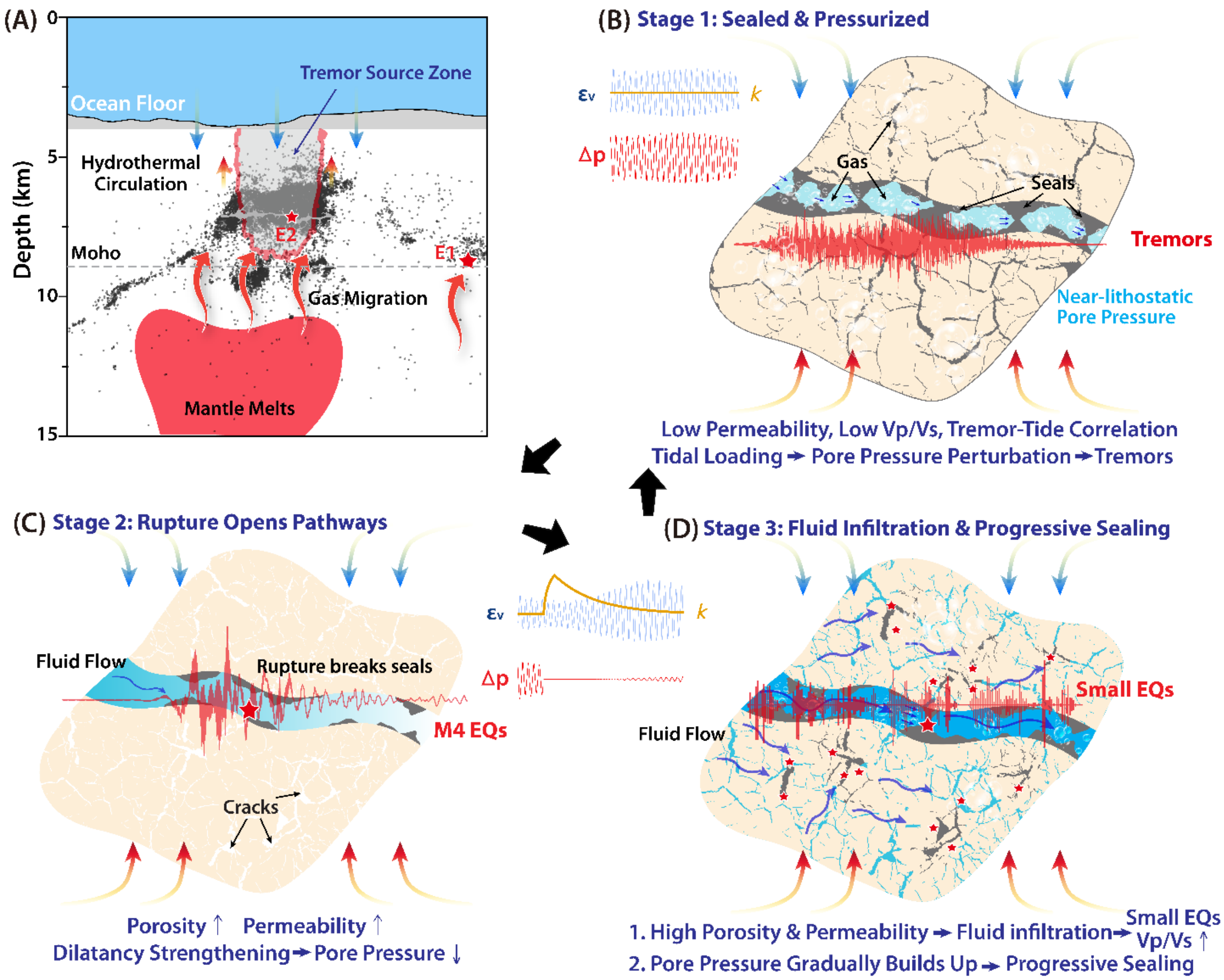

Fig. 5. Conceptual model for a shallow "sealing-pressurization-rupture" cycle on an oceanic transform fault. (**A**) Schematic cross section illustrating the relationship between subsurface seismicity (black dots), hydrothermal circulation (blue arrows), CO_2 degassing (gradational arrows), and deep mantle melt supply (red arrows) along the western segment (G3) of the Gofar transform fault (Fig. 1). Volatile-bearing fluids can migrate upward along the fault zone and modulate conditions within the seismogenic layer. Red stars show two M4 earthquakes (E1 and E2) on 11 August 2020 and 8 September 2020, respectively. The red contour indicates the tremor source zone. (**B** to **D**) Three-stage evolution cycle on a representative patch of the fault zone with a major flow path and small cracks in surrounding rocks. The temporal response of the pore pressure (Δp) to the volumetric strain (ε_v) of the tidal loading (fig. S18) is illustrated schematically for each stage, with the upper inset corresponding to Stage 1 and the lower inset showing the evolution across Stages 2 and 3. (B) Stage 1 sealed and pressurized: local mineral sealing reduces permeability and isolates a volatile-rich fluid phase, resulting in near-lithostatic pore pressure, such that small tidal stress perturbations can trigger harmonic tremors (tremor-tide correlation). Most cracks are sealed with some gas/fluid at this stage, and the permeability is low. (C) Stage 2 rupture opens pathways: moderate M4 earthquake ruptures break seals, open cracks, and rapidly increase permeability and porosity, leading to transient dilatancy strengthening and a local pore-pressure drop. (D) Stage 3 fluid infiltration and progressive sealing: fluid reinfiltrates cracks in the fault zone resulting in abundant microseismicity and high Vp/Vs; then as pore pressure gradually builds up, sealing resumes and progressively lowers permeability and Vp/Vs.

Cyclic sealing and drainage on an oceanic transform fault

Hao Yang, Lingling Ye, and Haijiang Zhang

Science **Ahead of Print** DOI: 10.1126/science.aed5665

Science (ISSN 1095-9203) is published by the American Association for the Advancement of Science. 1200 New York Avenue NW, Washington, DC 20005. The title *Science* is a registered trademark of AAAS.